Adaptive Kinematic and Dynamic Control for Hexapod Robots in Complex Construction Environments

Xiayu Zhao[1], Houtan Jebelli[1]

[1]Department of Civil and Environmental Engineering,
University of Illinois Urbana-Campaign, Champaign, IL, USA
xiayuz3@illinois.edu, hjebelli@illinois.edu

Abstract –

Robotic systems for inspection have advanced significantly in construction. Hexapod robots offer unique advantages for navigating complex construction terrains, yet their performance on sloped and irregular surfaces is hindered by limitations in existing control strategies. . In this work, we present an integrated control framework that combines a dynamically tuned fuzzy PD controller with a Bézier curve-based trajectory generator. This unified approach addresses the critical research gap by simultaneously ensuring precise posture regulation and smooth gait execution, thus enhancing hexapod stability and efficiency. Simulations in the Gazebo environment validated the system's performance on various roof pitches (2/12, 4/12, 6/12) and structural transitions (ridges, valleys, flashings). Results showed a 21% improvement in stability margin on 2/12 slopes, precise body orientation control within ±5° roll, ±10° pitch, and ±1.3 m/s² vertical acceleration variations. Also, this system achieved 80-100% success rates in three different types of surface transitions. This research provides a robust framework for deploying hexapod robots in challenging architectural contexts, advancing autonomous inspection capabilities in construction environments.

Keywords –

Robotic system; Hexapod Robots; Roof Inspection; Adaptive Kinematic Control; Complex Construction Environment; Autonomous Construction Inspection

1 Introduction

The construction industry is undergoing a transformative shift, propelled by the integration of robotic systems that streamline workflows and boost operational efficiency [1]. Among these applications, robotic systems developed for inspection tasks have advanced significantly, with researchers focusing on innovative locomotion methods that enable robots to navigate complex architectural structures [2,3]. Robots equipped with AI and computer vision are increasingly outperforming human capabilities in detecting and analysing maintenance needs, providing more accurate and timely assessments [4,5].

Despite these technological advancements, deploying robots for high-precision inspection tasks on construction sites remains challenging, often limiting their practical application [6]. Roof inspections, for instance, are particularly demanding due to diverse types of visible damage—curling, cracking, flaking, granule loss, and missing shingles—as well as less apparent issues, such as water infiltration, loosening, and blistering, which further complicate assessment [7]. To address these specialized inspection challenges, researchers have explored various robotic platforms with different locomotion mechanisms. Aerial robots, including Unmanned Aerial Vehicles (UAVs), offer potential solutions [8] but are constrained by payload capacity, battery life, and regulatory restrictions in urban settings, along with limited close-up inspection capabilities. Unmanned Ground Vehicles (UGVs) offer a viable alternative, as they support heavier payloads and can sustain longer operational times, making them more suitable for close-range inspections. However, standard UGVs often lack the adaptive locomotion needed to navigate the complex, sloped, and discontinuous surfaces commonly found on roofs, emphasizing the need for UGVs specifically designed for safe, slope-adaptive movement [9].

Among the various UGV configurations available for construction inspection tasks, multi-legged designs offer distinct advantages for complex terrain navigation. UGVs encompass various configurations, including wheeled, tracked, multi-legged, and hybrid forms, each with distinct advantages. Multi-legged UGVs excel on rough and uneven terrain [10]. Their ability to step over or around obstacles allows them to maneuver effectively in unstructured environments, making them well-suited for complex terrains. Multi-legged robots also offer greater agility, enabling movement in multiple directions, such as sideways and diagonally, which is particularly beneficial on sloped surfaces. Additionally, these designs ensure stability on downhill slopes by distributing load more effectively and provide resilience, allowing continued operation even with a compromised leg. Among multi-legged designs, hexapod robots stand out for their optimal balance between stability and complexity [11]. With six legs, they maintain static stability by keeping the Center of Gravity (CoG) within a support triangle formed by three legs, enabling a tripod gait that is both stable and efficient. This configuration provides redundancy, allowing the robot to function even if one or more legs malfunction, while avoiding the added complexity and energy demands of designs with more legs. Compared to quadrupeds, hexapods offer superior stability without requiring sophisticated dynamic balancing, as well as enhanced ground clearance and obstacle traversal. Furthermore, the hexapod design distributes load effectively, enabling the robot to carry heavier payloads while maintaining stability on uneven or inclined surfaces.

Despite these inherent advantages, hexapod robots still face challenges when navigating sloped and irregular terrains, as they often lack specialized kinematic and dynamic control mechanisms needed for such environments [12]. In applications like roof inspection, where safe and adaptive movement is critical, these gaps can lead to risks, including fall hazards [13], increased maintenance costs, and elevated energy consumption. This paper addresses this gap by proposing a novel integrated control framework that enhances both the kinematic and dynamic performance of hexapod robots. Our primary contributions include:

1. Providing an integrated control framework that synergistically combines an adaptive fuzzy PD controller and a Bézier curve-based trajectory generator. This unified approach dynamically adjusts leg motor angles based on center-of-gravity errors while generating smooth, energy-efficient swing-phase trajectories, resulting in superior posture regulation and enhanced stability on variable roof slopes and irregular terrains.
2. Validating the approach through extensive simulations, demonstrating a 21% improvement in stability margin on standard roof slopes and robust performance during complex structural transitions.

2 Methodology

This section presents a comprehensive description of the module-enhanced hexapod robot platform developed for automated roof inspection tasks.. This method adapt the traditional fuzzy PD controller with dynamic gain adjustments tailored for real-time leg motor control. Our study also extends the conventional use of Bézier curves by tuning the parameters for swing-phase trajectory generation. This results in smoother, energy-efficient leg movements that significantly improve gait stability over traditional semicircular trajectories. Furthermore, the novel aspect of our work is the integration of these two modified components into a unified control framework. This synergy not only leverages the strengths of both techniques but also produces superior performance,

2.1 Hexapod Kinematic Model

The hexapod robot platform utilized in this study is based on the model Muto [14], an 18 degrees-of-freedom (DoF) six-legged walking robot. The robot is equipped with a Jetson NANO board [15] for on-board processing. Locomotion is achieved through 18 high-torque servo motors. For precise posture measurement and adjustment, the robot incorporates an inertial measurement unit (IMU), capable of measuring acceleration, gyroscope data, magnetometer readings, and temperature. In default standing position, the hexapod robot measures 465 mm in length (forward direction) and 514 mm in width (lateral direction). Each of the six legs is composed of three segments: coxa (50 mm), femur (75 mm), and tibia (140 mm). The robot's coordinate frame is defined as shown in Fig.1(a): **{c}** is the mass center coordinate frame of hexapod robot determined by right-hand rule, with X_c along the body transverse direction, Y_c along the forward direction, and Z_c perpendicular to the ground. As shown in Fig.2(b), **{O_{ij}}** is the coordinate frame of the j_{th} joint of the i_{th} leg of the robot, $i \in \{1,2,3,4,5,6\}$, $j \in \{1,2,3,4\}$. Note when j=4, **{O_{i4}}** presents the coordinate frame of the foot end. Axis $\mathbf{Z_{i,j}}$ is the rotation axis of the joint, the $\mathbf{X_{i,j}}$ is chosen along the common normal from axes $\mathbf{Z_{i,j}}$ and $\mathbf{Z_{i,(j-1)}}$, and the $\mathbf{Y_{i,j}}$ is determined by righthand rule. Respectively, L1, L2, L3 represent the length of coxa (C_i), femur (F_i), and tibia (T_i), $i \in \{1,2,3,4,5,6\}$.

2.1.1 Forward Kinematics

The forward kinematics of the 18-DOF hexapod robot is based on the Denavit–Hartenberg (DH) convention. This approach allows for a systematic representation of the spatial relationships between adjacent link coordinate frames, facilitating the calculation of the end-effector position (in this case, the foot position) given the joint angles. The transformation matrix between two adjacent leg coordinate systems is

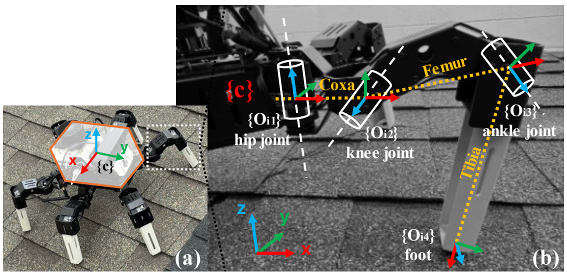

Figure 1. Kinematic Model of a Hexapod Robot Leg: Joints, Links, and Coordinate Frames

expressed in the DH convention:

$$\mathbf{M}_{\mathrm{j}}^{\mathrm{j-1}} = \begin{bmatrix} c_{\theta_j} & -s_{\theta_j}c_{\alpha_j} & s_{\theta_j}c_{\alpha_j} & \alpha_j c_{\theta_j} \\ s_{\theta_j} & c_{\theta_j}s_{\alpha_j} & -c_{\theta_j}s_{\alpha_j} & \alpha_j s_{\theta_j} \\ 0 & s_{\alpha_j} & c_{\alpha_j} & d_i \\ 0 & 0 & 0 & 1 \end{bmatrix} \quad (1)$$

where c_{θ_j}, s_{θ_j} denotes $\cos(\theta_j)$ and $\sin(\theta_j)$, respectively, and *α, a, θ, d* is the DH parameters with the values listed in Table 1.

Table 1. Denavit–Hartenberg Parameters Between **{c}** and the Hexapod's foot $\mathbf{p}_\mathbf{i}$

Transformation	α_i	a_i	θ_i	d_i
{c}→{O$_{i1}$}	0	l_l	θ_{il}	0
{O$_{i1}$}→{O$_{i2}$}	π/2	l_2	θ_{i2}	0
{O$_{i2}$}→{O$_{i3}$}	0	l_3	θ_{i3}	0
{O$_{i3}$}→{O$_{i4}$}	0	l_4	θ_{i4}	0

In Table 1, $\boldsymbol{\alpha}$ is the angle about common normal, from old z axis to new z axis; $\boldsymbol{a}$ is the length of the common normal; $\boldsymbol{\theta}$ is the angle about previous z from old x to new x; $\boldsymbol{d}$ is the offset along previous z to the common normal. Let $\mathbf{p}^c$ be the foot-tip position of the leg in the coordinate system relative to the mass center and $\mathbf{p}^4$ be the foot-tip position in the foot-tip coordinate system. Then the mapping between the body coordinate system and the foot-tip coordinate system is given by the following kinematic chain:

$$\mathbf{p}_\mathrm{i}^\mathrm{c} = \mathbf{T}_i^c\mathbf{M}_2^1\mathbf{M}_3^2\mathbf{M}_4^3\mathbf{p}_\mathrm{i}^4 \quad (2)$$

where $\mathbf{T}^\mathrm{i}$ is the transformation matrix between the body center frame **{c}** and the coxa coordinate frame of the i_{th} leg, given as a rigid body transformation:

$$\mathbf{T}^i = \begin{bmatrix} c_{\beta^i} & -s_{\beta^i} & 0 & p_x^i \\ s_{\beta^i} & -c_{\beta^i} & 0 & p_y^i \\ 0 & 0 & 1 & 0 \\ 0 & 0 & 0 & 1 \end{bmatrix} \quad (3)$$

where β^i, $\mathrm{p}_\mathrm{x}^\mathrm{i}$, and $\mathrm{p}_\mathrm{y}^\mathrm{i}$, are the body parameters of the i_{th} link which are known by default setting.

2.1.2 Inverse Kinematics

The inverse kinematics for the hexapod robot is simplified by its joint configuration, allowing for an analytical solution. Given the desired foot-tip coordinates in the global frame, the inverse kinematics calculates the required joint angles for each leg. For a given foot-tip position $\mathbf{p}^c = [\mathrm{p}_1^\mathrm{c}, \mathrm{p}_2^\mathrm{c}, \mathrm{p}_3^\mathrm{c}]$ in the global coordinates, the hip joint angle θ_1^i of the i_{th} is obtained as:

$$\theta_1^i = \begin{cases} 0, i = 1 \\ arctan\left(\frac{l_a}{l_b}\right), i \in \{2,3,5,6\} \\ \pi, i = 4 \end{cases} \quad (4)$$

where $\mathrm{l_a}$ and $\mathrm{l_b}$ are illustrated in Figure 2(a).

The angle θ_2^i is calculated with respect to the fixed reference frame $\{\mathbf{h}\}$ located at the **hip** joint (Fig. 1b):

$$\theta_2^i = \tan^{-1}\left(\frac{x_p^h}{y_p^h}\right) \quad (5)$$

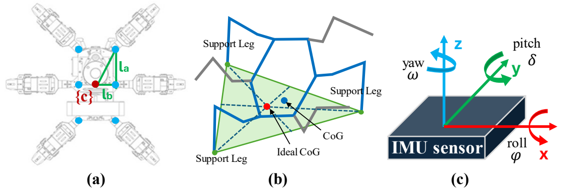

Figure 2. (a) Hip Joint Relative to the Center Frame, (b) Diagram Explaining CoG and CSP, (c) Rotation Angles Measured by the IMU Sensor

where $\mathbf{p}_\mathrm{i}^\mathrm{h} = \{x_p^h, y_p^h, z_p^h\}^T$ is the position of $\mathbf{p}_\mathrm{i}$ relative to $\{\mathbf{h}\}$, obtained by:

$$\mathbf{p}_\mathrm{i}^\mathrm{h} = (\mathbf{T}_1^0)^{-1}\mathbf{p}_\mathrm{i}^\mathrm{c} \quad (6)$$

in which $\mathbf{T}_1^0$ is the transformation matrix between the center frame $\{\mathbf{c}\}$ and the reference frame $\{\mathbf{h}\}$. To calculate the remaining angles, we need the position of reference frame $\{\mathbf{k}\}$ at the knee joint, defined by the Denavit-Hartenberg convention as:

$$\mathbf{k}_\mathrm{i}^\mathrm{h} = (\mathbf{T}_1^0)^{-1}\mathbf{T}_2^0 \quad (7)$$

Considering the vector $\mathbf{s}_\mathrm{p}$ between the knee frame $\{\mathbf{k}\}$ and the foot, the angle θ_3^i and the θ_4^i are calculated as:

$$\theta_3^i = \cos^{-1}\left(\frac{{l_3}^2 + \|\boldsymbol{s}_p\|^2 - {l_4}^2}{2l_3\|\boldsymbol{s}_p\|}\right) - \sin^{-1}\left(\frac{z^k - z^p}{\|\boldsymbol{s}_p\|}\right) \quad (8)$$

$$\theta_4^i = \pi + \cos^{-1}\left(\frac{{l_3}^2 + {l_4}^2 - \|s_p\|^2}{2l_3 l_4}\right) \quad (9)$$

z^k and z^p represent the vertical positions of the knee frame $\{\mathrm{k}\}$ and the foot, respectively. These equations form the foundation for the robot's motion control and gait design in subsequent sections.

2.2 Integrated Control System for Slope and Terrain Stability

2.2.1 Adaptive Control System for Slope Navigation

The stability of a hexapod robot during locomotion on both inclined and uneven surfaces is crucial for effective roof inspection tasks. This section presents an integrated approach that combines slope-adaptive posture control with enhanced gait stability mechanisms to ensure reliable operation across diverse terrain conditions. The foundation of the system's stability is based on the principle that the hexapod robot maintains static stability when the vertical projection of its Center of Gravity (CoG) falls within the Conservative Support Polygon (CSP) formed by its supporting legs (Fig. 2b). While this principle is straightforward on flat surfaces where the D-H convention and forward kinematics can directly calculate support points and CoG projection, inclined surfaces present additional complexity as the robot's reference frame **{c}** becomes misaligned with the global reference frame **{s}.** To address this misalignment, a rotation matrix is introduced to transform positions from the robot's reference frame **{c}** to the space reference frame **{s}**:

$$\mathbf{R_{sc}} = \begin{bmatrix} c_\omega c_\delta & c_\omega s_\delta s_\varphi - s_\omega c_\varphi & c_\omega s_\delta c_\varphi + s_\omega s_\varphi & 0 \\ s_\omega c_\delta & s_\omega s_\delta s_\varphi + c_\omega c_\varphi & s_\omega s_\delta c_\varphi - c_\omega s_\varphi & 0 \\ -s_\delta & c_\delta s_\varphi & c_\delta c_\varphi & 0 \\ 0 & 0 & 0 & 1 \end{bmatrix} \quad (10)$$

where the rotation angles φ around X-axis, δ around Y-axis, and ω around Z-axis are measured by the IMU sensor (Fig. 2c) positioned at the robot's center of mass.

Stability on inclined surfaces is further improved using a fuzzy Proportional-Derivative (PD) controller, which dynamically adjusts the supporting leg motors' angles. This study chooses the fuzzy PD controller for three main reasons: (1) it handles the nonlinearities and uncertainties of slope navigation without requiring a precise dynamic model, (2) it dynamically adjusts control parameters based on error magnitude and rate of change, ensuring better adaptation to varying slopes, and (3) it strikes an optimal balance between performance and computational efficiency, essential for real-time embedded systems in field robotics. The controller maintains the real CoG's projection close to the ideal CoG within the CSP by calculating errors e_x and e_y, representing differences between the actual and ideal CoG positions. The compensation angles $\Delta\mu_x$ and $\Delta\mu_y$ are calculated as:

$$\Delta\mu_x = K_{p,x} e_x + K_{d,x} \dot{e}_x \quad (11)$$

$$\Delta\mu_y = K_{p,y} e_y + K_{d,y} \dot{e}_y \quad (12)$$

where $K_{p,x}$ and $K_{p,y}$ are the proportional gains, $K_{d,x}$ and $K_{d,y}$ are the derivative gains, all of which are dynamically adjusted by the fuzzy PD controller based on the magnitude of errors and their derivatives [16]. This approach allows the system to respond appropriately to varying conditions. For instance, when errors are large, smaller gains are applied to prevent the robot from overturning. Conversely, when errors are small, larger gains are used for fine-tuning motor adjustments, enhancing stability (Table 2,3., Figure 3).

Table 2. Consequent membership Functions

Parameter \ Value	↑	↑↑	↑↑↑	↑↑↑↑
$K_{p,x}$	0.05	0.1	0.15	0.2
$K_{p,y}$	0.2	0.3	0.4	0.5
$K_{d,x}$	0.05	0.07	0.09	0.15
$K_{d,y}$	0.05	0.07	0.09	0.15

Table 3. Fuzzy rule table for the proportional and derivative gains

$K_{p,x}$ / $K_{d,y}$	$K_{p,y}$ / $K_{d,x}$	e_y: − −	−	0	+	+ +
$\dot{e}_y$	− −	↑	↑↑	↑↑↑	↑↑	↑
	−	↑↑	↑↑↑	↑↑↑↑	↑↑↑	↑↑
	0	↑↑↑	↑↑↑↑	↑↑↑↑	↑↑↑↑	↑↑↑
	+	↑↑	↑↑↑	↑↑↑↑	↑↑↑	↑↑
	+ +	↑	↑↑	↑↑↑	↑↑	↑

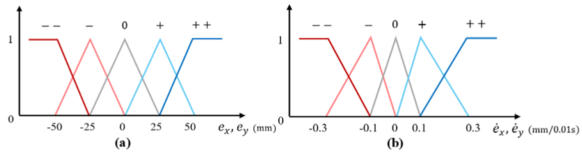

Figure 3. Fuzzy rule plots for e_x, e_y and $\dot{e}_x$, $\dot{e}_y$

In practice, the global reference frame rotates with the robot's reference frame around the Z-axis to ensure that compensation angles remain effective regardless of the robot's orientation. The fuzzy PD controller's ability to adapt dynamically outperforms traditional linear PD controllers, particularly on inclined surfaces, by maintaining stability without detailed dynamic modelling. This adaptive control strategy was validated through experiments on roof pitches of varying slopes, detailed in the *Experimental Validation* section.

2.2.2 Stability Enhancement for Uneven Terrain

The robot employs a tripod gait as its primary locomotion strategy, where three legs remain in the stance phase while the other three are in the swing phase. The legs are divided into two sets: Set A (legs R1, L2, and R3) and Set B (remaining legs). This configuration enables a four-step sequence: initial six-foot contact (Fig. 4a), Set A forward movement (Fig.4b), Set B forward movement with Set A thrust (Fig.4c), and Set A lift returning to initial position (Fig.4d). The swing leg trajectory is the curve connecting the lifting point and the landing point of the swing leg's tip.

Traditionally, a semicircular trajectory algorithm is used for the swing phase, generating uniform foot arcs. While computationally efficient, this method produces abrupt transitions between the stance and swing phases, increasing energy consumption and destabilizing the robot's posture. To mitigate these issues, this study introduces a Bézier curve-based trajectory for the swing phase. This method, modelled as a third-degree curve, ensures more consistent height control during the swing phase. This study chose Bézier curves over polynomial, spline, and semicircular trajectories for three main reasons: (1) control points enable smoother stance-to-swing transitions, (2) Bézier curves avoid the oscillations typical of high-order polynomials and maintain stability under varying terrain conditions, and (3) they strike an optimal balance between trajectory quality and computational efficiency.

During the swing phase, the feet follow a 3rd-degree

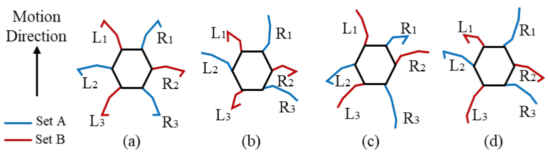

Figure 4. Diagram of four-step tripod gait

Bézier trajectory described by:

$$\mathbf{p}_{i,j}^{c}(t) = \sum_{j=0}^{3} \binom{3}{j} t^{j}(1-t)^{3-j}\mathbf{p}_{i,j}^{c}\,,$$
$$t \in [0, t_{int}], i \in [1,6], j = 0,1,2,3 \quad (13)$$

$$\binom{3}{j} = \frac{3!}{j!\,(3-j)!} \quad (14)$$

where 3 denotes the curve degree, j denotes the number of joint, t_{int} is the trajectory's time interval, and $\mathbf{p}_{i,j}^{c} = \{x_p^c, y_p^c, z_p^c\}^T$ denote the control points of the trajectory.

This approach provides superior stability compared to traditional methods, particularly in terms of roll and pitch velocity variation and height stability. The control points for the Bézier curve are strategically positioned to ensure smooth transitions between phases while maintaining stability. The first control point corresponds to the foot's initial position $\mathbf{p}_{i,0}^{c}$ is defined by Eq. (2), which can also be derived as:

$$\mathbf{p}_{\mathrm{i},0}^{\mathrm{c}} = \begin{Bmatrix} c_{(\theta_0+\theta_1)}(L_3 c_{(\theta_2+\theta_3)} + L_2 c_{\theta_2} + L_1) + L_0 c_{\theta_0} \\ s_{(\theta_0+\theta_1)}(L_3 c_{(\theta_2+\theta_3)} + L_2 c_{\theta_2} + L_1) + L_0 s_{\theta_0} \\ L_3 s_{(\theta_2+\theta_3)} + L_2 s_{\theta_2} \end{Bmatrix} \quad (15)$$

The remaining control points are determined as:

$$\mathbf{p}_{\mathrm{i},1}^{\mathrm{c}} = \left\{0, \frac{s}{4}, \frac{h}{3}\right\}^{\mathrm{T}} + \mathbf{p}_{\mathrm{i},0}^{\mathrm{c}} \quad (16)$$

$$\mathbf{p}_{\mathrm{i},2}^{\mathrm{c}} = \left\{0, \frac{3s}{4}, \frac{h}{3}\right\}^{\mathrm{T}} + \mathbf{p}_{\mathrm{i},0}^{\mathrm{c}} \quad (17)$$

$$\mathbf{p}_{\mathrm{i},3}^{\mathrm{c}} = \{0, s, 0\}^{\mathrm{T}} + \mathbf{p}_{\mathrm{i},0}^{\mathrm{c}} \quad (18)$$

where *h* is the maximum height, and *s* denotes the stride length. During the stance phase, where the feet maintain ground contact while propelling the torso forward, the foot trajectory is defined as:

$$\mathbf{p}_{\mathrm{i}}^{\mathrm{c}}(\mathrm{t}) = \left\{0, -\frac{s}{t_{int}}t, 0\right\}^{\mathrm{T}} + \mathbf{p}_{\mathrm{i},0}^{\mathrm{c}}, t \in [0, t_{int}] \quad (19)$$

By integrating slope-adaptive posture control with a stability-enhanced gait system, this approach addresses the dual challenges of inclined and uneven terrain navigation. The adaptive slope system ensures that the CoG remains properly aligned within the CSP, while the Bézier curve trajectory smooths leg movements, enhancing stability and energy efficiency.

3 Experimental Validation

The experimental validation of the proposed control system was conducted through two comprehensive simulation tests implemented in the Gazebo environment, each designed to evaluate different aspects of the hexapod robot's performance. The simulation environment was configured using Robot Operating System (ROS) and Gazebo, providing a physics-accurate testing platform. The same hexapod robot URDF (Unified Robot Description Format) model was employed across both test setups, ensuring consistency in the robot's physical parameters and joint configurations throughout the experimentation process. Gazebo and ROS together provide a comprehensive and flexible setup for simulating and measuring with the appropriate sensors, plugins, and ROS nodes.

3.1 Test 1: Diverse Slopes

Test 1 evaluated the control system's stability across various roof inclines using the tripod gait, which balances stability and speed at 0.1 m/s. Three standard residential roof pitches were tested: 2/12 (9.5°), 4/12 (18.4°), and 6/12 (26.6°). The simulation used a 3.0m × 2.0m platform with high-friction coefficient (μ = 0.8) to simulate roofing material. For each slope, the hexapod performed five ascending trials covering 3.0m distance.

The robot model incorporated an IMU sensor at its center of mass, providing orientation data through ROS "sensor_msgs" for accurate CoG projection calculations. Performance metrics included stability margin, body orientation angles, foot placement accuracy, and power consumption. The simulation featured realistic physics parameters to ensure accurate representation of the robot's behavior on inclined surfaces. For all experiments, we implemented a comparative analysis between our integrated control system and a traditional control approach. The baseline system utilized a standard PD controller with fixed gains (Kp = 0.5, Kd = 0.15) for posture regulation and conventional semicircular trajectory generation for leg movements.

3.2 Test 2: Surface Transitions

Test 2 evaluated the control system's ability to navigate common roof structural transitions using the same hexapod model from Test 1. The simulation focused on three critical elements: ridge lines (30° angular transition), valleys (135° angles), and flashings (10mm elevation change).

For each transition type, ten trials were conducted at 0.1 m/s from identical start positions to ensure statistical reliability. Data was collected using the robot's integrated sensors, including IMU readings for stability assessment and foot pressure sensors for contact force analysis.

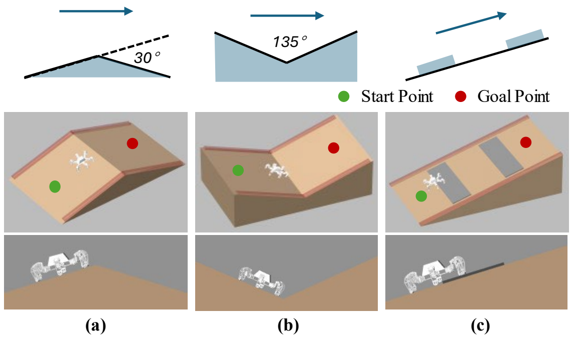

Figure 6. Three different surface transition trials in Test 2: (a) Ridge (30 degree), (b) Valley (135 degree), (c) Flashing (10mm elevation).

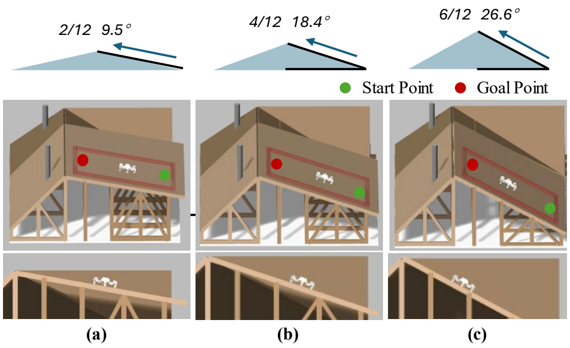

Figure 5. Three different slope angle trials in Test 1: (a) Pitch 2/12 (~9.5 degree), (b) Pitch 4/12 (~18.4 degree), (c) Pitch 6/12 (~26.6 degree).

Performance evaluation concentrated on two key metrics: transition success rate and crossing time.

3.3 Performance Metrics

To comprehensively evaluate the hexapod robot's performance across both slope navigation and structural transition tests, a multi-metric evaluation framework was implemented. The primary stability indicator was the stability margin (SM), defined as the shortest distance from the horizontally projected Center of Gravity (CoG) to the edge of the support polygon (McGhee and Frank 1968):

$$S_m \equiv \min(D_1, D_2, D_3)$$

where D_i represents the perpendicular distance from the projected CoG to each edge of the support triangle formed by the supporting legs. This metric has been extensively validated in previous studies for analysing hexapod stability [17] and designing fault-tolerant gaits [16]. Body orientation control was monitored through roll (φ) and pitch (θ) angles, measured in degrees from the horizontal plane. The maximum allowable deviations were established at 15° for roll angle, 20° for pitch angle on slopes, and 12° for pitch angle during structural transitions. These measurements were crucial for assessing the robot's ability to maintain proper posture throughout locomotion.

For Test 1 (Diverse Slopes), specific performance metrics included: (1) Average stability margin maintained during continuous slope walking; (2) Maximum and minimum body orientation angles during slope traversal; (3) Vertical Acceleration variations. For Test 2 (Surface Transitions), additional metrics were implemented: (1) Transition success rate, defined as the percentage of crossings completed without stability failures such as turnover or keep stepping in place; (2) Crossing time, measured from the initiation of transition approach to completion of crossing from fixed start and end positions. All metrics were recorded through the ROS framework using custom message types, with data synchronized through the ROS time stamp system. The results are analysed in the following section.

4 Results and Discussion

4.1 Results Analysis

4.1.1 Test 1: Diverse Slopes Performance

The experimental results revealed significant stability gains with our control system for all tested slope angles (Figure 7), namely 2/12 (9.5°), 4/12 (18.4°), and 6/12 (26.6°). On the gentlest slope, the system maintained an average SM of 115 mm, 21% higher than the default. Although this margin dropped to 84 mm at 4/12 pitch, it still surpassed the default by 15%. On the steep 6/12 pitch, our system recorded 44 mm—over double the 20 mm minimum for stable locomotion—while the default system repeatedly overturned or stepped in place. These results highlight the inherent challenges of steep inclines, which our adaptive control strategy successfully mitigated. Overall, we achieved a 100% success rate, with only brief interruptions during initial slope engagement.

Body orientation control also showed strong performance (Figure 8). Our system maintained body height between 255 and 272 mm, while the uncontrolled approach varied from 228 to 289 mm, especially on steeper slopes. Roll angles stayed within ±2°, ±3°, and ±5° at 9.5°, 18.4°, and 26.6°, respectively—well below the ±15° limit. By contrast, the default approach reached ±15° on the 6/12 pitch. Pitch angles similarly stayed within ±10° under our system, far beneath the 20° cutoff, while the default reached ±25°. The fuzzy controller's adaptive nature minimized sudden orientation changes, containing vertical acceleration within ±1.3 m/s², whereas the uncontrolled approach hit ±2.5 m/s². These findings confirm the robust stabilization capabilities of our system on inclined surfaces.

Such improvements in stability and orientation are critical for preventing slip or rollover events. By minimizing abrupt shifts, our system reduces mechanical stress and power consumption, enabling safer, more efficient navigation and real-world roof inspections. Hence, it effectively supports steep-roof applications requiring reliable locomotion.

4.1.2 Test 2: Surface Transition Performance

As shown in Table 4, the system demonstrated high success rates across all structural surface transitions, with 80% successful completions for ridge line crossings (30° angle) among 10 trials, compared to 50% success rate without our control system. Under another 10 trails on valley transitions (135° angle), trails under our control system gained 100% success, while only 6 of another 10 trails succeeded without our control system. For flashing interface navigation (10mm elevation change), both trails

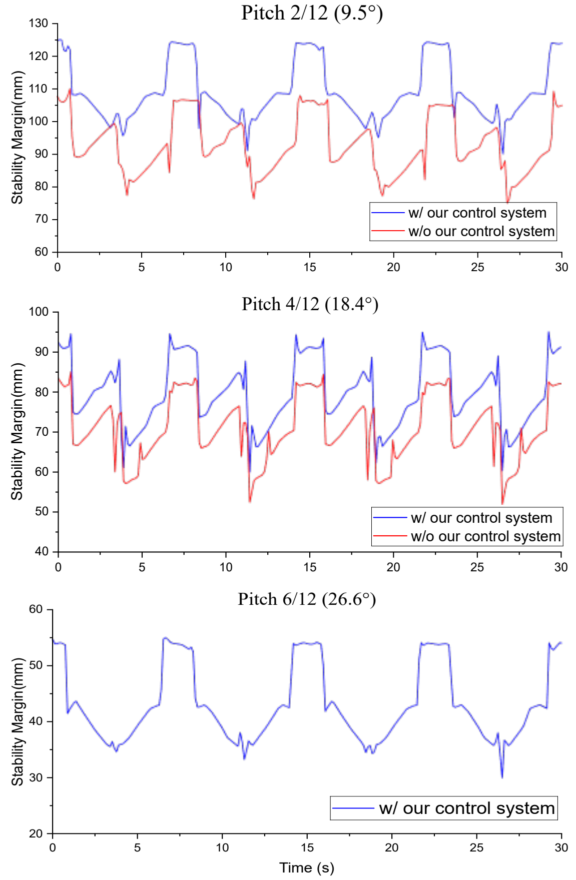

Figure 7. Stability Margin Comparison w/ and w/o Our Control System on Pitch 2/12, 4/12, and 6/12.

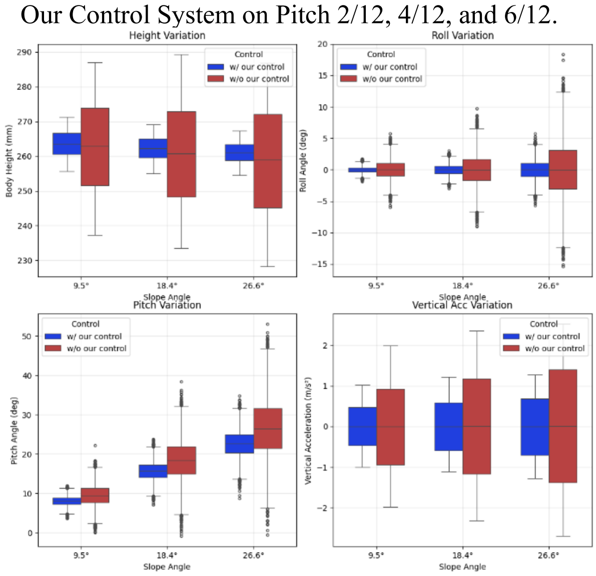

Figure 8. Orientation (Height, Roll, and Pitch) Variation and Acceleration Variation on Pitch 2/12, 4/12, and 6/12

w/ and w/o our control system achieved 100% success rate, but the trails without our control system had trouble with stepping in place for a while before going through the transition area, which lead to longer task complete time. The average crossing times shown in Table 1 varied significantly by transition type: 8.6 seconds (w/ our control system) and 11.5 seconds (w/o our control system) for ridge lines; 5.7 seconds (w/ our control system) and 6.8 seconds (w/o our control system) for valleys; 7.7 seconds (w/ our control system) and 8.9 seconds (w/o our control system) for flashing interfaces.

Table 4. Result Metrics of Test 2

Subtest	Transition Type	Success Rate (%)		Average Crossing Time (s)	
		w/ ours	w/o ours	**w/ ours**	w/o ours
#1	ridge	**80%**	50%	**8.6**	11.5
#2	valley	**100%**	60%	**5.7**	6.8
#3	flashing	**100%**	100%	**7.7**	8.9

4.2 Discussion

The results of Test 1 and Test 2 demonstrate that our integrated control system significantly enhances hexapod robot performance in both slope navigation and structural transition scenarios.

In Test 1, the system demonstrated enhanced stability across different roof slopes, with notable improvements in stability margin and body orientation control compared to the default control system. The use of a fuzzy PD controller was instrumental in maintaining consistent body orientation, particularly in challenging inclines. The improvement becomes more crucial at steeper angles, as demonstrated by the system's ability to maintain stable locomotion on 6/12 pitch slopes where default controls failed. The ability to maintain roll and pitch angles within acceptable limits highlights the system's robustness, allowing for effective traversal of various roof pitches without compromising stability. The Bézier curve-based gait trajectory further contributed to a smoother and more energy-efficient movement, reducing abrupt transitions that could destabilize the robot.

Test 2 focused on the hexapod robot's ability to navigate structural transitions commonly encountered during roof inspections, such as ridges, valleys, and flashings. The high success rates achieved across different transition types (80% for ridge lines, 100% for valleys) represent a marked improvement over conventional control methods. The reduced crossing times for all transition types indicate that our system not only improves success rates but also enhances efficiency. This is particularly evident in flashing interface navigation, where both control systems achieved 100% success rates, but our system demonstrated superior efficiency in transition completion times. The fuzzy PD controller's dynamic adjustments ensured that the robot could adapt its posture in real-time, thereby mitigating risks associated with sudden changes in terrain. The Bézier curve-based trajectory also played a crucial role in ensuring smooth foot placement during these transitions, reducing the likelihood of slips or missteps.

However, certain limitations were observed during testing. The slight decrease in stability margin with increasing slope angle suggests that additional optimization may be needed for extremely steep slopes. Furthermore, the 80% success rate in ridge line crossings, while superior to conventional methods, indicates room for improvement in handling sharp angular transitions.

5 Conclusion

This research presents an adaptive control system for hexapod robots that improves stability in complex construction environments. By integrating a fuzzy PD controller with a Bézier curve-based trajectory generator, our system maintains stability across varied terrain. This work advances construction robotics in three significant ways: (1) it demonstrates how intelligent control strategies can overcome traditional limitations of ground robots on variable construction surfaces, (2) it provides a validated framework for autonomous inspection in previously challenging environments, reducing human exposure to hazardous conditions, and (3) it establishes quantifiable performance benchmarks for robotic systems in construction inspection tasks, creating a foundation for future developments in this domain. The findings highlight the potential for deploying hexapod robots in challenging construction environments, extending beyond roof inspections to other applications that require adaptive locomotion on irregular or inclined surfaces, such as structural health monitoring of bridges, post-disaster building assessment, and maintenance of complex industrial facilities.

Future work will focus on further refining the control algorithms, including exploring machine learning-based adaptations to enhance real-time decision-making and developing a more robust physical prototype for field testing. Additionally, we plan to investigate energy efficiency improvements to extend operational time, thereby enhancing the practicality of hexapod robots for prolonged inspection and maintenance tasks. Although our evaluations were performed in the Gazebo simulation environment, these results offer a robust preliminary assessment of our method while minimizing associated risks and costs. Future work will involve validating our approach through controlled real-world experiments to further substantiate its practical applicability and performance.

References

[1] S. Shayesteh, H. Jebelli, Toward Human-in-the-Loop Construction Robotics: Understanding Workers' Response through Trust Measurement during Human-Robot Collaboration, Construction Research Congress 2022: Computer Applications, Automation, and Data Analytics - Selected Papers from Construction Research Congress 2022. 2-B (2022) pp. 631–639. https://doi.org/10.1061/9780784483961.066.

[2] D. Lattanzi, G. Miller, Review of Robotic Infrastructure Inspection Systems, Journal of Infrastructure Systems. 23 (2017) pp. 04017004. https://doi.org/10.1061/(ASCE)IS.1943-555X.0000353.

[3] H. Peel, S. Luo, A.G. Cohn, R. Fuentes, Localisation of a mobile robot for bridge bearing inspection, Automation in Construction. 94 (2018) pp. 244–256. https://doi.org/10.1016/j.autcon.2018.07.003.

[4] X. Zhao, H. Jebelli, A computational method for real-time roof defect segmentation in robotic inspection, Computer-Aided Civil and Infrastructure Engineering. (2025). https://doi.org/10.1111/MICE.13471.

[5] A. Khan, C. Mineo, G. Dobie, C. Macleod, G. Pierce, Vision guided robotic inspection for parts in manufacturing and remanufacturing industry, Journal of Remanufacturing. 11 (2021) pp. 49–70. https://doi.org/10.1007/s13243-020-00091-x.

[6] Y. Liu, H. Jebelli, Enhanced Robotic Teleoperation in Construction Using a GAN-Based Physiological Signal Augmentation Framework, Lecture Notes in Civil Engineering. 239 (2023) pp. 295–307. https://doi.org/10.1007/978-981-19-0503-2_24.

[7] H. Miura, T. Aridome, M. Matsuoka, Deep Learning-Based Identification of Collapsed, Non-Collapsed and Blue Tarp-Covered Buildings from Post-Disaster Aerial Images, Remote Sensing. 12 (2020) pp. 1924. https://doi.org/10.3390/rs12121924.

[8] P. Sestras, G. Badea, A.C. Badea, T. Salagean, S. Roșca, S. Kader, F. Remondino, Land surveying with UAV photogrammetry and LiDAR for optimal building planning, Automation in Construction. 173 (2025) pp. 106092. https://doi.org/10.1016/J.AUTCON.2025.106092.

[9] X. Zhao, T. Ren, H. Jebelli, Adaptive Intelligence for Robot Navigation Efficiency with a Deep-Reinforcement-Learning-Based Cyber-Physical System, in: 2024 International Conference on Computing in Civil Engineering (I3CE), 2024.

[10] L. Yang, P. Li, S. Qian, H. Quan, J. Miao, M. Liu, Y. Hu, E. Memetimin, Path Planning Technique for Mobile Robots: A Review, Machines 2023, Vol. 11, Page 980. 11 (2023) pp. 980. https://doi.org/10.3390/MACHINES11100980.

[11] J. Coelho, F. Ribeiro, B. Dias, G. Lopes, P. Flores, Trends in the Control of Hexapod Robots: A Survey, Robotics 2021, Vol. 10, Page 100. 10 (2021) pp. 100. https://doi.org/10.3390/ROBOTICS10030100.

[12] Y. Liu, C. Wang, H. Zhang, J. Zhao, Research on the Posture Control Method of Hexapod Robot for Rugged Terrain, Applied Sciences 2020, Vol. 10, Page 6725. 10 (2020) pp. 6725. https://doi.org/10.3390/APP10196725.

[13] A. Ojha, Y. Liu, S. Shayesteh, H. Jebelli, W.E. Sitzabee, Affordable Multiagent Robotic System for Same-Level Fall Hazard Detection in Indoor Construction Environments, Journal of Computing in Civil Engineering. 37 (2023). https://doi.org/10.1061/(ASCE)CP.1943-5487.0001052.

[14] Muto S2 Robot, (n.d.). http://www.yahboom.net/study/Muto-S2 (accessed November 16, 2024).

[15] NVIDIA, Jetson Nano, (n.d.). https://developer.nvidia.com/embedded/jetson-nano (accessed November 16, 2024).

[16] Z.Y. Wang, X.L. Ding, A. Rovetta, Analysis of typical locomotion of a symmetric hexapod robot, Robotica. 28 (2010) pp. 893–907. https://doi.org/10.1017/S0263574709990725.

[17] Jung-Min Yang, Jong-Hwan Kim, Fault-tolerant locomotion of the hexapod robot, IEEE Transactions on Systems, Man and Cybernetics, Part B (Cybernetics). 28 (1998) pp. 109–116. https://doi.org/10.1109/3477.658585.